Materials & Design 260 (2025) 114976

Contents lists available at ScienceDirect

Materials & Design

journal homepage: www.elsevier.com/locate/matdes

Dynamic compression of sinusoidal plate lattices: Energy absorption and failure characteristics

Piyapat Jameekornkul, Ajit Panesar *

IDEA Lab, Department of Aeronautics, Imperial College London, SW7 2AZ, UK

ARTICLE INFO

Keywords:
Lattice structures
Dynamic behaviour
Sinusoidal geometry
Strain-rate sensitivity

ABSTRACT

Plate-based lattices have emerged as promising candidates for lightweight structural and energy-absorbing applications; however, the latter remain largely underexplored. This study investigates the quasi-static and dynamic compressive behaviour of BCC and FCC plate lattices featuring a novel sinusoidal plate geometry. Lattices were additively manufactured in ABS and tested across strain rates from 0.001 to 43.5 s^{-1}. The sinusoidal geometry promoted stable deformation by suppressing localised failure in both plate lattices, albeit with reduced stiffness and strength. Compared to BCC, sinusoidal FCC lattices exhibited pronounced strain-rate strengthening, likely owing to the increased strain-rate sensitivity of bulk ABS under shear loading. A Cowper–Symonds plasticity model provided robust dynamic strength predictions across strain rates. These findings underscore the potential of sinusoidal plate lattices for tailored energy absorption and deformation control in additively manufactured structures.

1. Introduction

Architected cellular materials are increasingly employed in lightweight structures where high specific stiffness and efficient energy absorption are critical, such as aerospace panels [1], biomedical implants [2], and impact-protection systems [3]. Their appeal stems from the ability to tailor performance through geometric design combined with additive manufacturing (AM) capabilities, extending beyond material composition alone [4]. Among various lattice architectures, plate-based lattices, recently proposed by Berger et al. [5], have gained interest due to their high stiffness and strength, approaching theoretical upper bounds for isotropic materials (i.e., the Hashin–Shtrikman and Suquet bound [5,6]). However, despite their superior theoretical mechanical performance, the closed-cell configurations of plate lattices are susceptible to powder entrapment during powder-based AM processes [7]. Material extrusion (MEX) addresses this issue through layer-by-layer deposition whilst offering low production costs [8,9].

The thin-walled plate members comprising plate lattices are susceptible to panel buckling prior to yielding. This has driven research into geometric modifications aimed at delaying or stabilising buckling while preserving their lightweight benefits. Reported strategies include hybrid lattices [10–12], plate perforations [13,14], and computationally optimised designs [15]. Sinusoidal corrugation has been extensively adopted in 2D sandwich panels [16,17] and thin-walled tubes [18], and recently has been applied to 3D lattice structures for enhanced buckling resistance in truss-based lattices [19], grids [20] and plate-based lattices [21,22]. Derveni et al. [22] observed that sinusoidal perturbations can stabilise and strengthen low-density plate lattices but may lead to premature plastic collapse at higher relative densities, where bifurcation occurs near yield. Similarly, Ding et al. [21] reported that mild corrugations improve post-buckling performance and energy absorption at low relative density (<4.7 %). Nevertheless, it remains unclear whether such sinusoidal modifications remain beneficial for buckling stability in denser lattices under dynamic loading conditions.

The dynamic behaviour of lattice structures at intermediate strain rates remains insufficiently characterised [23], with dynamic loading introducing stress gradients, strain rate-dependent material behaviour, and localised deformation that can alter failure mechanisms [24,25]. Most dynamic studies on plate-based lattices have focused on metallic system [24,26–28], where Tancogne et al. [28] demonstrated that constituent material strain rate sensitivity drives lattice's performance. However, as metals and polymers differ in their elastic–plastic transitions and energy dissipation mechanisms, these findings are less directly applicable to polymer-based lattices. Existing research by Andrew et al. [29,30] has addressed polymer plate-based lattice behaviour through drop-weight impact evaluations, examining the effects of impact energy,

* Corresponding author.
E-mail address: a.panesar@imperial.ac.uk (A. Panesar).

https://doi.org/10.1016/j.matdes.2025.114976
Received 21 July 2025; Received in revised form 13 October 2025; Accepted 18 October 2025
Available online 22 October 2025
0264-1275/© 2025 The Authors. Published by Elsevier Ltd. This is an open access article under the CC BY-NC-ND license (http://creativecommons.org/licenses/by-nc-nd/4.0/).

carbon nanotube reinforcement, and cell topology. Nevertheless, the effects of geometric modifications and strain rate remain unstudied. This lack of data restricts the utilisation of polymer lattices for controlled deformation and impact energy absorption.

This study investigates how sinusoidal geometries alter the compressive response and failure mechanisms of plate lattices under both quasi-static and dynamic loading. Through experimental campaigns and theoretical analysis, modified Body-centred cubic (BCC) and face-centred cubic (FCC) plate lattices are compared against their conventional flat-plate counterparts. This comparison elucidates the complex interplay between failure mode, geometric modification, and strain-rate sensitivity. The findings advance the understanding of how tailored geometric features govern dynamic failure, offering new insights to design principles for crashworthiness of AM cellular structures.

2. Methodology

2.1. Design of flat and sinusoidal plate lattices

To investigate the effect of sinusoidal features, both flat (i.e., conventional) plate lattices and modified sinusoidal versions were created. BCC and FCC variants were selected due to their prevalence in prior research and their comparable truss-based counterparts, where struts and plates are arranged in the same cubic crystal structures [6,26]. Additionally, both topologies are self-supporting, making them well-suited to the MEX-AM process.

The arrangement of plates within the BCC and FCC cells follows the design principles established by Tancogne-Dejean et al. [6], in which crystallographic planes are used to define plate orientations. Miller index notation was employed to describe the plate families (Fig. 1) [31], where an index of zero indicates that the plane is parallel to the corresponding axis. The z-axis was designated as the build direction to align with the layer-wise fabrication process. In this convention, the BCC cell consists of six rectangular plates aligned with the {110} family of planes (i.e. {011}, {101}, {110}), while the FCC cell consists of four hexagonal plates corresponding to the {111} family, each inclined at an angle of $\phi = 55^\circ$ and rotated by $\theta = 45^\circ$, 135°, 225°, and 315° to form a symmetric enclosure within the cube's bounding volume. These FCC plates are connected at the corners by eight triangular elements.

A parametric framework was developed using Python and OpenSCAD. Flat plates were first defined as surface matrices in Python, then imported into OpenSCAD where they were oriented, combined to form a unit cell, and tessellated along the x-, y-, and z-axes into $3 \times 3 \times 3$ lattices for mechanical testing, a size commonly used in prior studies as a practical balance between representativeness and experimental feasibility [29,32,33]. In the sinusoidal lattices, each flat plate was modified into a bi-directional sinusoidal surface, defined as:

$$d = A\sin\left(2\pi f_x \frac{x}{L}\right)\sin\left(2\pi f_y \frac{y}{L}\right) \quad (1)$$

where x and y denotes spatial coordinates and L is the plate length. The amplitude A and frequency f(with $f_x = f_y = f$, unless stated otherwise) are tuneable descriptors. A preliminary study (Appendix B) confirmed that f influences yield strength and plateau stress fluctuations. However, as the aim was to isolate the effect of sinusoidal shaping, both parameters are fixed in this study. The adopted values ($A = 1.125$ mm, $f = 1$, $L = 7.5$ mm) reflect MEX feature-size limits and unit-cell dimensions, ensuring that deformation mechanisms were clearly observable during experiments. Fig. 2 shows the resulting flat and sinusoidal BCC and FCC configurations.

2.2. Fabrication and materials

The fabrication process was carried out using MEX technique on an Ultimaker S5 printer [34], employing Acrylonitrile Butadiene Styrene (ABS) filament. A layer height of 0.15 mm, solid infill setting, and build direction (z-axis in Fig. 2) were fixed, whilst the standard ABS temperature profile for the Ultimaker was used. A quality assessment was performed using dimensional measurements, weight analysis, and optical microscopy to ensure consistency in fabrication.

To investigate the effect of relative density (i.e. ratio of the density of the lattice to its constituent) on mechanical properties, three relative densities (ρ) were considered: 0.35, 0.5, and 0.65. The relative density was varied by adjusting the plate thickness, while maintaining a constant unit cell edge length of 7.5 mm. Both flat and sinusoidal plate unit cells were tessellated into a $3 \times 3 \times 3$ lattice structure. The is fixed It should be noted that slight differences in plate thickness may be observed between configurations, as maintaining consistent ρ was prioritised across all samples.

A test matrix was designed to systematically capture the influence of key design parameters, including ρ, cell type, sinusoidal features, and loading condition. Each configuration was tested with at least four repeats under both quasi-static and dynamic loading. The test cases included two lattice types (FCC and BCC) and two plate configurations (flat and sinusoidal). The breakdown of these test configurations is summarised in Table 1.

3. Experimental procedure

3.1. Quasi-static testing

Quasi-static compression tests were conducted using a 50 kN Instron universal testing machine at a nominal strain rate of 0.001 s^{-1}. A preload of 50 N (~1% of the expected yield stress [35]) was applied to ensure uniform contact between the specimen and the compression platens. Digital Image Correlation (DIC), providing an independent validation of global strain and enabling local strain field visualisation throughout loading.

The stress–strain response was computed from the obtained force-

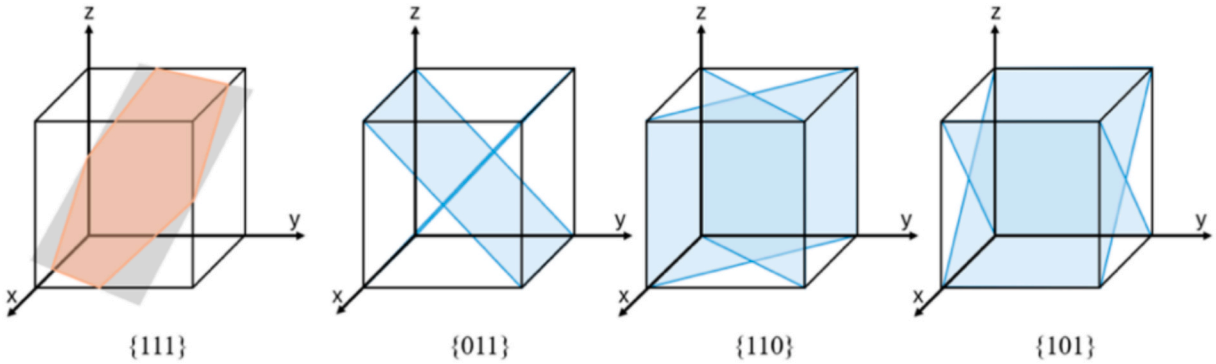


Fig. 1. Miller's index [31] of the plates forming the plate-based lattice structures.

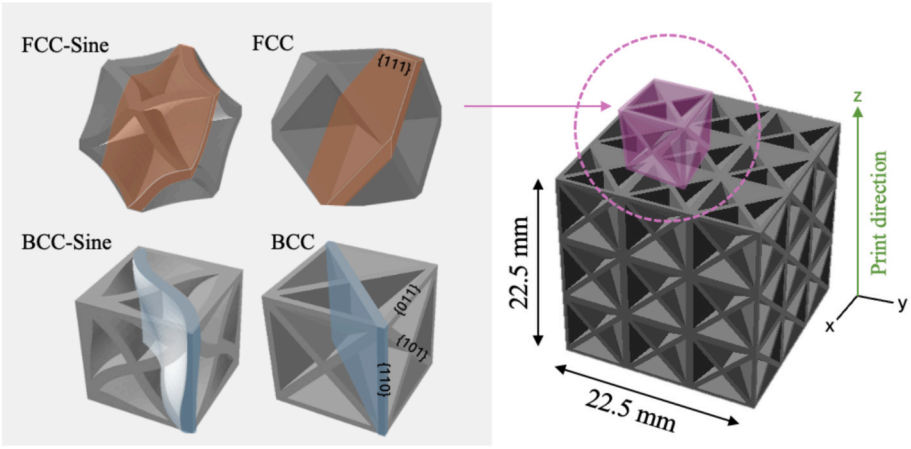


Fig. 2. Dimensions and visualisations of flat and sinusoidal plate lattice structures.

Table 1
Testing matrix.

Cell Type	Feature	Loading Condition	Relative Densities (ρ)
BCC/FCC	Flat/Sinusoidal	Quasi-static Dynamic	0.35/0.5/0.65 0.35

–displacement ($F-\delta$) data using the nominal cross-sectional area and initial height of each specimen, along with standard deviation (SD) bands reported across repeats. The elastic modulus (E) was determined from the linear portion of the stress–strain curve within the strain range of 0.05–0.2. The yield stress ($\sigma_{y,qs}$) was evaluated using the 0.2 % offset method following standard procedure [36].

To enable meaningful comparison between lattice configurations of varying relative density (ρ), both stiffness and yield strength were normalised by the corresponding values of the base material. These bulk material properties were obtained from compression testing of fully dense reference samples fabricated under identical process conditions ($E_0 = 1.22$ GPa and $\sigma_{y,0} = 56$ MPa, validated with previous study [37]).

Unless stated otherwise (e.g. for comparison with previous studies), all energy absorption (E_a) was computed by integrating the $F-\delta$ curve up to their own densification onset strain (ε_{D0}). The densification strain was defined using the energy efficiency function, $\kappa(\varepsilon)$, as follows:

$$\kappa(\varepsilon) = \frac{1}{\sigma(\varepsilon)} \int_0^{\varepsilon} F(\varepsilon) d\varepsilon \tag{2}$$

The ε_{D0} corresponds to the strain at which the slope of $\kappa(\varepsilon)$ approaches zero, signifying the transition from progressive deformation to compaction-dominated collapse. This method provides a robust and objective criterion for identifying the onset of densification. For comparative analysis across different relative densities (ρ), the normalised energy absorption ($\widehat{E_a}$) was computed as :

$$\widehat{E_a} = \frac{\int_0^{\varepsilon_{D0}} F(\varepsilon) du}{\rho} = \frac{E_a}{\rho} \tag{3}$$

The analytical estimation of buckling strength for isolated flat plates under prescribed boundary conditions was used to guide experimental interpretation. These derivations were based on the theory of elastic stability [38,39] and plate crushing mechanics [40,41], and were subsequently compared against experimentally observed failure behaviour.

3.2. Dynamic testing

Dynamic tests were performed using an Instron CEAST 9350 drop-weight impact machine with a 90 kN load cell and a 100 mm flat impactor. Impact energies were varied by adjusting the drop height and weight. A Phantom high-speed camera (10,000 fps) captured ~ 100 frames per test to observe failure progression.

To ensure impact velocities remained within the intermediate strain rate regime and below the onset of wave-dominated effects, a critical velocity threshold was estimated based on the elastic wave speed of ABS ($49.7 m/s$, Appendix A). Through preliminary trails and errors, impact energies of 15 J and 60 J were selected (Table 2), the corresponding average strain rates.

were 22.2 and 43.5 s^{-1}, respectively, both within the targeted intermediate strain rate regime (1–100 s^{-1}). V.

The contact force (F) and time (t) data were analysed in accordance with ASTM D7136 [42], from which impactor displacement $\delta(t)$ and energy absorption $E_a(t)$ profiles were extracted. The specific energy absorption (SEA) of the lattice was determined as the remaining absorbed energy after the impact event per lattice's mass (Eq. (4)).

Depending on the loading condition, the free-fall impactor either bounced back, transferring residual kinetic energy away from the lattice, or remained in contact, inducing further deformation. Additionally, the ε_{D0} was determined using the same approach as in quasi-static compression or, alternatively, identified as the strain at which the contact force reached zero, indicating full energy dissipation.

To assess strain rate effects, the Dynamic Increase Factor (DIF) was computed using Eq. (5) as the ratio of dynamic yield stress to quasi-static.

$$SEA_d = \frac{E_a}{m} \tag{4}$$

$$DIF = \frac{\sigma_{y,d}}{\sigma_{y,qs}} \tag{5}$$

4. Results

4.1. Quasi-static compressive curves

4.1.1. Baseline flat plate lattice

As shown in Fig. 3a and b, the quasi-static compression behaviour of flat plate lattices follows a typical three-stage response for cellular materials: linear elasticity, a stress plateau, and densification [43].

Table 2
Drop weight impact testing parameters.

Impact energy [J]	Drop height [mm]	Drop weight [kg]	Impact velocity [m/s]
15	58.57	26.1	1.07
60	234.3	26.1	2.14

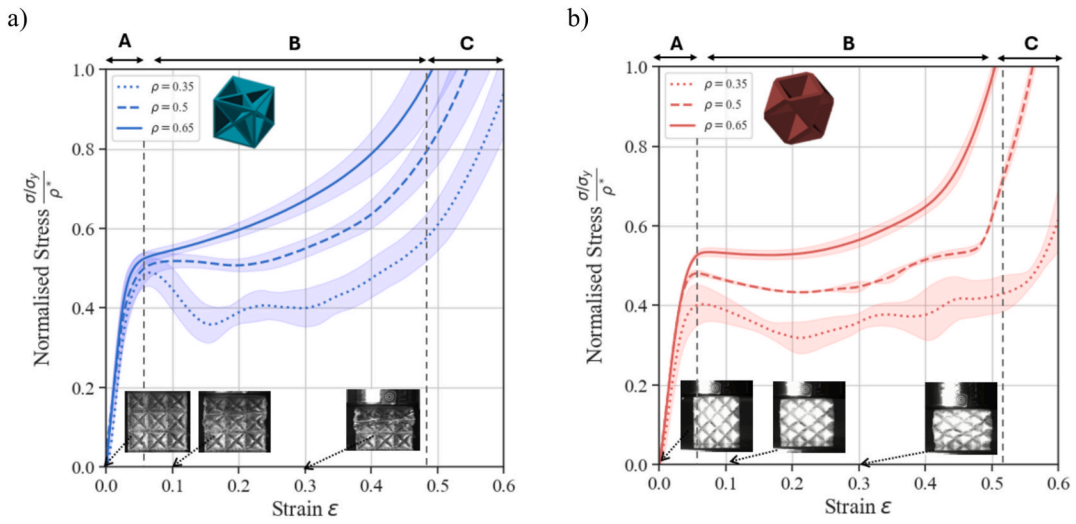


Fig. 3. Normalised stress–strain curves for a) BCC flat plate and b) FCC flat plate at $\rho = 0.35, 0.5, 0.65$. Regions A, B and C correspond to the linear-elastic, plateau and densification stages, respectively, in the $\rho = 0.35$ sample.

Effective stiffness and strength both demonstrated a clear power-law relationship with $\rho(R^2 > 0.92)$, with all fitted coefficients detailed in Appendix A [44].

The variation between repeated tests, represented by the standard deviation (SD) shaded regions, increased as the ρ decreased. This effect also reflected differences in failure mode, with the SD for BCC lattices (Fig. 3a) being wider than that for FCC lattices (Fig. 3b) at $\rho \geq 0.5$. Although the BCC and FCC topologies exhibited comparable stiffness

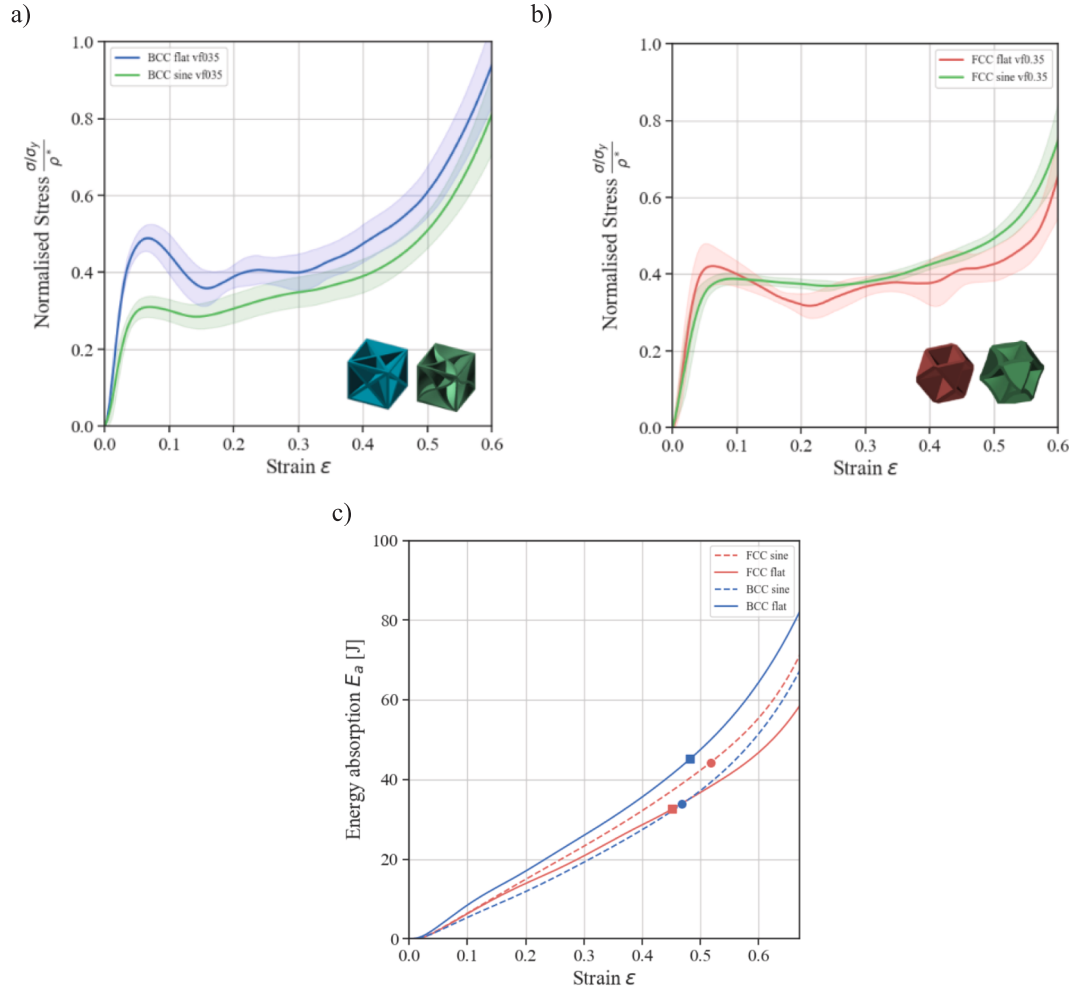


Fig. 4. Normalised stress–strain curves for a) BCC and b) FCC lattices comparing flat and sinusoidal feature (all at fixed $\rho = 0.35$), and c) corresponding energy absorption for each configuration.

and plateau stress at low relative densities, their performance diverged as ρ increased. At the highest ρ tested, the BCC configuration showed notably greater stiffness and strength.

4.1.2. Sinusoidal plate lattice

Fig. 4 compares the stress–strain responses of sinusoidal and flat plate lattices at $\rho = 0.35$. Qualitatively, the flat lattices exhibit more pronounced stress fluctuations in the plateau region, whereas the sinusoidal lattices show a smoother stress profile with less variation across the strain range, particularly for the FCC topology. The key mechanical properties derived from these curves are summarised in Table 3. The data shows that in both BCC and FCC configurations, the sinusoidal structures exhibit lower stiffness and strength than their flat counterparts, with the reduction being more pronounced in BCC lattices.

The introduction of the sinusoidal geometry also delayed the onset of densification (ε_{D0}) compared to the flat counterparts, with the FCC sinusoidal lattice showing the greatest delay ($\Delta\varepsilon_{D0} = 0.07$). Corresponding energy absorption values ranged from 43.22 J to 53.71 J, with FCC sinusoidal lattices exhibiting the highest energy absorption. These performance differences remain despite the reported error margins ($< 5\%$), reflecting the influence of sinusoidal geometry on the deformation response.

4.1.3. Dynamic response of flat and sinusoidal plate lattices

Initial peak force and deformation behaviour varied with lattice configuration. A significant reduction in peak force was observed for the sinusoidal BCC lattices compared to their flat counterparts (Fig. 5a), whereas the FCC lattices showed only a slight reduction (Fig. 5b).

Following this primary peak, the force–displacement curves of the flat configurations were characterised by a sharp drop, while the sinusoidal lattices exhibited a more gradual decline in load-bearing capacity. Despite these differences in the force–displacement response, the total energy absorption was comparable across all configurations, with each dissipating over 95 % of the initial impact energy.

5. Discussion

5.1. Performance and failure of baseline (flat) lattices

5.1.1. Effect of cell topology and relative density

Subjected to quasi-static loading, the FCC lattice exhibits a distinct stress plateau typical of cellular solids [43], whereas the BCC lattice shows a more gradual stress increase with strain (Fig. 3a and b). At the lowest tested relative density ($\rho = 0.35$), stress–strain curves present fluctuations within the plateau regions, resulting from local instabilities such as thin-plate buckling in both topologies. Increasing ρ and corresponding plate thickness leads to a smoother plateau behaviour. The BCC lattices exhibit a slightly larger stress drop from yield to plateau compared with the FCC, qualitatively consistent with the behaviour of BCCP lattices reported in [12].

Theoretical upper bounds, specifically the Hashin-Shtrikman (HS) [45] and Suquet [46] models, served as a reference for the stiffness and yield strength of isotropic cellular solids (Fig. 6a and 6b, respectively). Plate lattices approached these bounds and outperform other lattice types, including surface-based [5,11] and truss-based structures [43,47]. This experimental observation aligns with recent numerical studies [5,8]. To further confirm that the scaling behaviour is predominantly governed by geometry rather than the constituent material, Onyx BCC results were cross-validated against other materials, showing < 4 % difference in the fitted exponents.

BCC lattices exhibited superior relative stiffness and yield strength compared to FCC, attributed to two key factors. Firstly, the vertically aligned {1 1 0} plates in the BCC structure provide efficient axial load transfer, thereby increasing stiffness and strength [48]. Secondly, BCC lattices exhibit higher geometric fidelity via MEX, due to their alignment with the build direction. Conversely, the angled plates in FCC lattices are more susceptible to fabrication inaccuracies, which likely accounting for discrepancies between experimental results and numerical predictions for FCC [8].

Regarding failure mechanisms, it should be noted that whilst BCC lattices benefit from axial load transfer through vertically aligned plates, the complete BCC geometry also contains oblique {1 1 0} plates and edge-sharing arrangements that introduce bending and shear as strain increases, giving rise to scaling exponents slightly above unity and indicating a mixed response. By contrast, FCC lattices comprise oblique hexagonal plates whose plate connectivity constrains out-of-plane bending and promotes in-plane membrane stresses along shared edges, consistent with prior findings [8]. This results in an effective stretching-dominated response, with exponents close to unity.

Energy absorption (E_a) follows a power-law relationship with ρ. As shown in Fig. 6c, plate lattices absorb more energy than previously reported Schwarz-P (SP) architectures at the same ρ and ε_{D0} [42]. Under quasi-static loading, the E_a varies only slightly across topologies. Note that several factors contribute to this accumulated energy, including plateau stress, densification behaviour and the strain at densification onset, all of which depend on the governing failure mechanism and may vary with material choice. A detailed examination of these failure mechanisms and their associated mechanical properties is thus warranted.

5.1.2. Analytical prediction

Buckling and collapse of component plates govern the failure mechanisms in both BCC and FCC lattices. In BCC specimens, the initial instability appears at the centre of the vertical {1 1 0} plates (Fig. 9), aligning with the lowest-order buckling prediction based on classical plate theory (CPT) [38]. Building on CPT and Derveni et al.'s framework [22], the critical elastic buckling stresses of a component plate are expressed in Eqs. (6) and (7). The term $1/cos^2\phi$ accounts for the 55° inclination angle of FCC plates, and the geometry factors $C_{BCC} = 3.70$ and $C_{FCC} = 4.44$ relate the plate slenderness ratio to relative density.

$$\sigma_{cr}^{BCC} = xk\frac{\pi^2 E}{12(1-\nu^2)}\left(\frac{\rho}{C_{BCC}}\right)^2 \tag{6}$$

$$\sigma_{cr}^{FCC} = xk\frac{\pi^2 E}{12(1-\nu^2)}\left(\frac{\rho}{C_{FCC}}\right)^2 \times \frac{1}{cos^2\phi} \tag{7}$$

$$\rho_{crit} = C\sqrt{\frac{12(1-\nu^2)}{xk\pi^2}} \times \sqrt{\frac{\sigma_Y}{E}} = C\sqrt{\frac{12(1-\nu^2)}{xk\pi^2}} \times M \tag{8}$$

Considering plastic deformation by setting $\sigma_{crit} = \sigma_Y$ in Eqs. (6) and (7), the critical density ρ_{crit} is defined by Eq. (8). This value scales linearly with the material index, M. Replacing a high-strength metal ($M = 0.07$) by ABS ($M = 0.21$), triples the critical densities, predicting ρ_{crit} values of

Table 3
Averaged mechanical properties of quasi-static compression test.

Lattices	Stiffness [MPa]	Strength [MPa]	Onset strain ε_{D0}	Energy absorption [J]
BCC sinusoidal	191.87 ± 5.0 %	3.93 ± 1.5 %	0.52 ± 2.4 %	43.22 ± 4.0 %
BCC flat	270.31 ± 2.1 %	5.59 ± 3.3 %	0.49 ± 2.2 %	46.28 ± 3.4 %
FCC sinusoidal	218.86 ± 3.3 %	4.32 ± 4.1 %	0.58 ± 3.7 %	53.71 ± 2.8 %
FCC flat	265.99 ± 1.9 %	5.24 ± 2.6 %	0.51 ± 3.6 %	50.15 ± 2.1 %

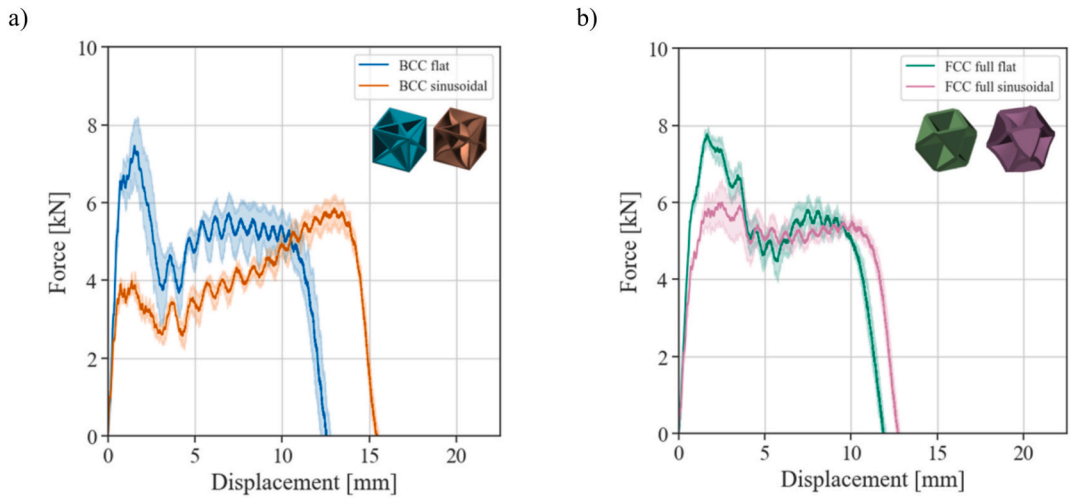


Fig. 5. Force–displacement curves from a 60 J impact at flat and sinusoidal plate lattice: a) BCC and b) FCC lattices (For 15 J results, see Figure B1).

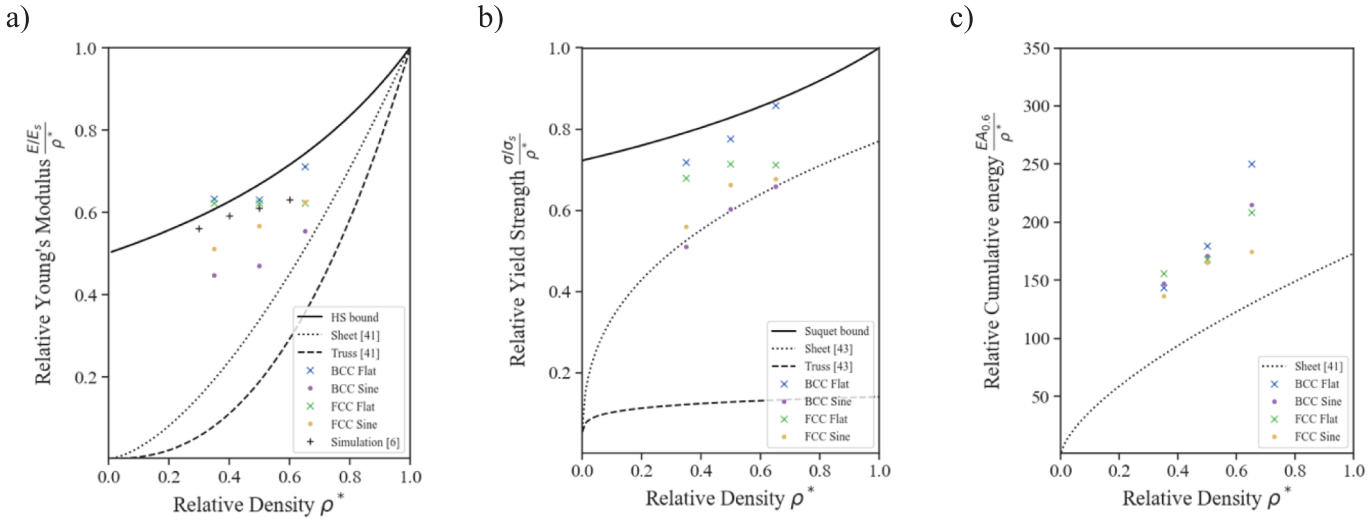


Fig. 6. Relative mechanical properties in comparison to literatures and theoritical bounds a) relative modulus b) yield stress and c) cumulative absorbed energy.

0.34 for BCC and 0.24 for FCC. Above these thresholds, the failure mechanism transitions from elastic buckling to plastic yielding or localised fracture.

Consistent with these predictions, the BCC lattice at $\rho = 0.35$ (slightly above its ρ_{crit} of 0.34) shows a continuous stress rise without a stiffness drop in elastic region (i.e., region A in Fig. 3a). Conversely, the FCC lattice, tested above its critical density enters plastic collapse at lower strain, exhibiting a shorter elastic regime and flatter plateau

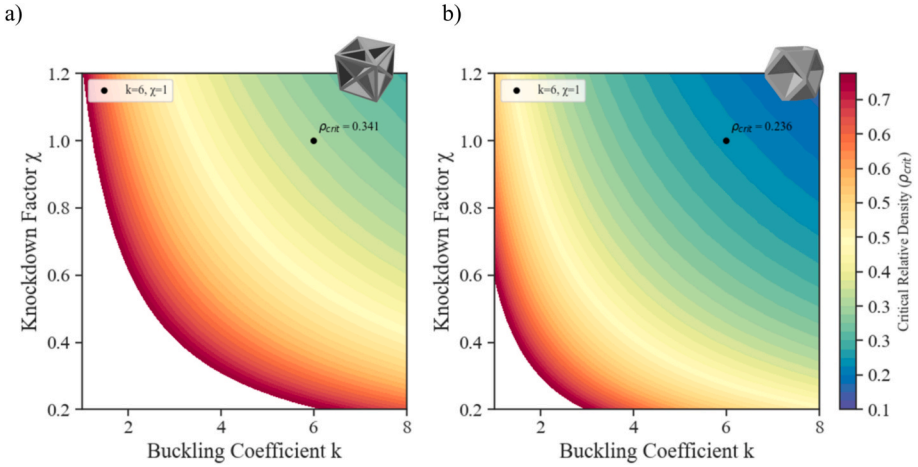


Fig. 7. Relative critical buckling stress a) BCC and b) FCC with variations in *k* and *x*.

(Fig. 3b). These behaviours confirm the transition from buckling-dominated to yield-dominated response for $\rho > \rho_{crit}$.

When plates are assembled into a full lattice structure, shared edges and multiple intersecting nodes enhance boundary stiffness, increasing the buckling coefficient k up to ~ 8 [22,49]. A higher k lowers the predicted ρ_{crit} relative to isolated plates (Eqs. (6) to (8)). Conversely, manufacturing defects typically reduce the knock-down factor $x < 1$, thus increasing ρ_{crit} [50]; however, this detrimental effect usually remains smaller than the stiffening effect from shared edges. Consequently, the isolated-plate model provides a conservative lower bound. Fig. 7 illustrates the combined impact of variations in k and x for each lattice topology.

Corrugated plate enhances plate compliance, thereby reducing overall load carrying capability. According to [51], this effect can be quantified by multiplying σ_{crit} by a chord-to-arc length ratio, which is less than one for curved plates and unity for flat plates. This adjustment effectively captures the reduced buckling strength in sinusoidal plates due to increased compliance and potentially capture the threshold for the sinusoidal plate lattices.

However, the simplified plate model assumptions inadequately represent localised failure mechanisms, including inter-layer delamination, vertical cracking, or rotation at junctions. These defects can interrupt the post-buckling load transfer and precipitate premature collapse. Accurate predictions of σ_{crit} thus require more detailed modelling and comprehensive experimental validation that account for both global deformation and local damage evolution.

5.1.3. Effect of strain rate

The dynamic yield stress $(\sigma_{y,d})$ of all specimens increased with applied strain rate $(\dot{\varepsilon})$, as reflected by the increasing values of the dynamic increase factor (DIF), defined as the ratio of $\sigma_{y,d}$ to $\sigma_{y,qs}$ (Table 4). Among flat-plate configurations, BCC and FCC exhibited differing DIF increases, owing to their distinct deformation mechanisms. BCC cells deform mainly via axial compression of vertical {110} plates, directly translating the polymer's strain-rate sensitivity into higher structural strength. In contrast, FCC cells deform primarily through bending and shear of inclined {111} plates [8,52], dampening this effect. Similar trends are observed in other lattice architectures, with truss-based BCC structures exhibiting higher DIF values [53] than surface-based gyroids [54]. Despite the increased severity, failure modes resemble those observed quasi-statically; therefore, scaling relationships (Appendix C) are expected to persist with higher scaling coefficients whilst exponent values should remain consistent [25,55,56].

The introduction of sinusoidal features altered the deformation behaviour distinctly in each topology. In BCC lattices transitioned from axial compression to a more compliant bending-dominated deformation mode thereby reducing the stiffness and flattening the $\sigma_{y,d} - \dot{\varepsilon}$ curves. As a result, sinusoidal BCC lattices yielded the lowest DIF values across all configurations. Conversely, the sinusoidal FCC lattices showed enhanced $\sigma_{y,d}$, surpassing their flat counterparts at $\dot{\varepsilon} > 40s^{-1}$ (Fig. 8). This can be attributed to the suppression of local plate failure, which promoted a more uniform stress distribution under shear-dominated global deformation. Given that bulk ABS shows increased $\dot{\varepsilon}$ sensitivity under shear [57], this uniform more likely facilitated greater engagement of shear-driven $\dot{\varepsilon}$ effects, thereby elevating $\sigma_{y,d}$.

Table 4
Yield strength and DIF values for flat and sinusoidal plate lattices under varying strain rates.

Configuration	UC type	$\dot{\varepsilon} = 0.001$ $\sigma_{y,qs}$	$\dot{\varepsilon} = 22.2$ σ_{y,d_15J}	$\dot{\varepsilon} = 43.5$ σ_{y,d_60J}	DIF_{15J}	DIF_{60J}
Flat	BCC	5.59	11.28	13.45	2.02	2.41
	FCC	5.24	9.20	10.67	1.76	2.04
Sinusoidal	BCC	3.93	6.21	6.63	1.58	1.69
	FCC	4.32	7.77	11.02	1.80	2.55

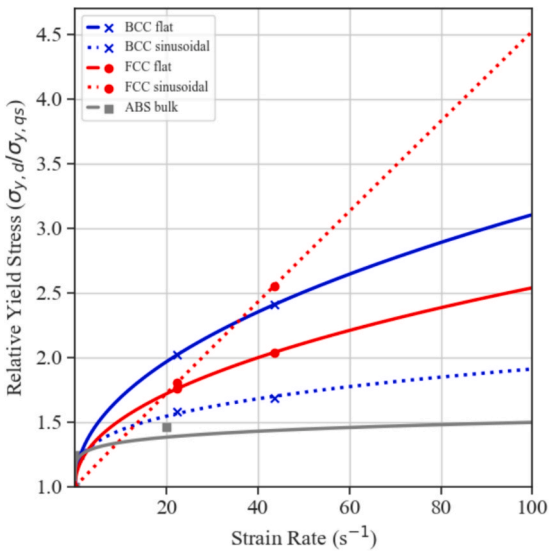


Fig. 8. Normalised yield stress $(\frac{\sigma_{y,d}}{\sigma_{y,qs}})$ over strain rate range compared to bulk ABS [37].

The Cowper–Symonds model (Eq. (9) [58]) fitted the experimental data effectively, yielding $R^2 > 0.94$ values across all configurations. Predicted $\sigma_{y,d}$ at a $\dot{\varepsilon} = 34\ s^{-1}$ closely matched the experimental results for the 45 J impact case (excluded from the fitting), with differences within 5 %. The contribution of inertial effects (represented by the third term in Eq. (9)) was considered negligible due to low impact velocity (v) involved in the intermediate $\dot{\varepsilon}$ regime tested.

$$\sigma_{y,d} = \sigma_{y,qs} + \sigma_{y,qs}\left(\frac{\dot{\varepsilon}}{a}\right)^{\frac{1}{b}} + \frac{\rho_0 v^2}{\varepsilon_d} \tag{9}$$

The quasi-static strength $(\sigma_{y,qs})$ is known to be governed by the dominant failure mode through power-law coefficients. In the dynamic regime, $\sigma_{y,d}$ builds upon this $\sigma_{y,qs}$ baseline, incorporating an additional dependence on $\dot{\varepsilon}$ through parameters a and b in Eq. (9). Although all specimens were fabricated from the same ABS material, the fitted values of a and b varied across lattice configurations (Appendix C). This indicates that the dominant failure mode not only sets the quasi-static baseline but also dictates the dynamic performance of the structure. For comparison, the Johnson-Cook formulation [59] was fitted using the same dataset and assumptions, though the prediction error at a $\dot{\varepsilon} = 34\ s^{-1}$ was higher ($\sim$9%). The corresponding fitted coefficients are provided in Table C2.

The observed topology- and $\dot{\varepsilon}$-dependent behaviour directly informs design implications: flat BCC lattices excel in low strain-rate applications; sinusoidal FCC lattices provide superior performance in high $\dot{\varepsilon}$ condition; and sinusoidal BCC provides the most rate-agnostic response across the tested strain rates.

6. Influence of sinusoidal geometry

6.1. Failure mechanisms: Quasi-static regime

Under quasi-static compression, the flat BCC lattice ($\rho = 0.35$) exhibited folding of vertical {1 1 0} plates. This folding created plastic hinges at mid-span, which acted as rotational failure points and led to splitting between printed layers (Fig. 9). Delamination was also evident between the upper and middle lattice unit cell layers, likely due to insufficient interlayer bonding. These localised failure mechanisms induced pronounced strain concentrations, as evident in the DIC strain fields (ε_{xx} and ε_{zz}, Fig. 10), particularly in the upper half of the specimen.

Conversely, the sinusoidal BCC lattice exhibited a more distributed

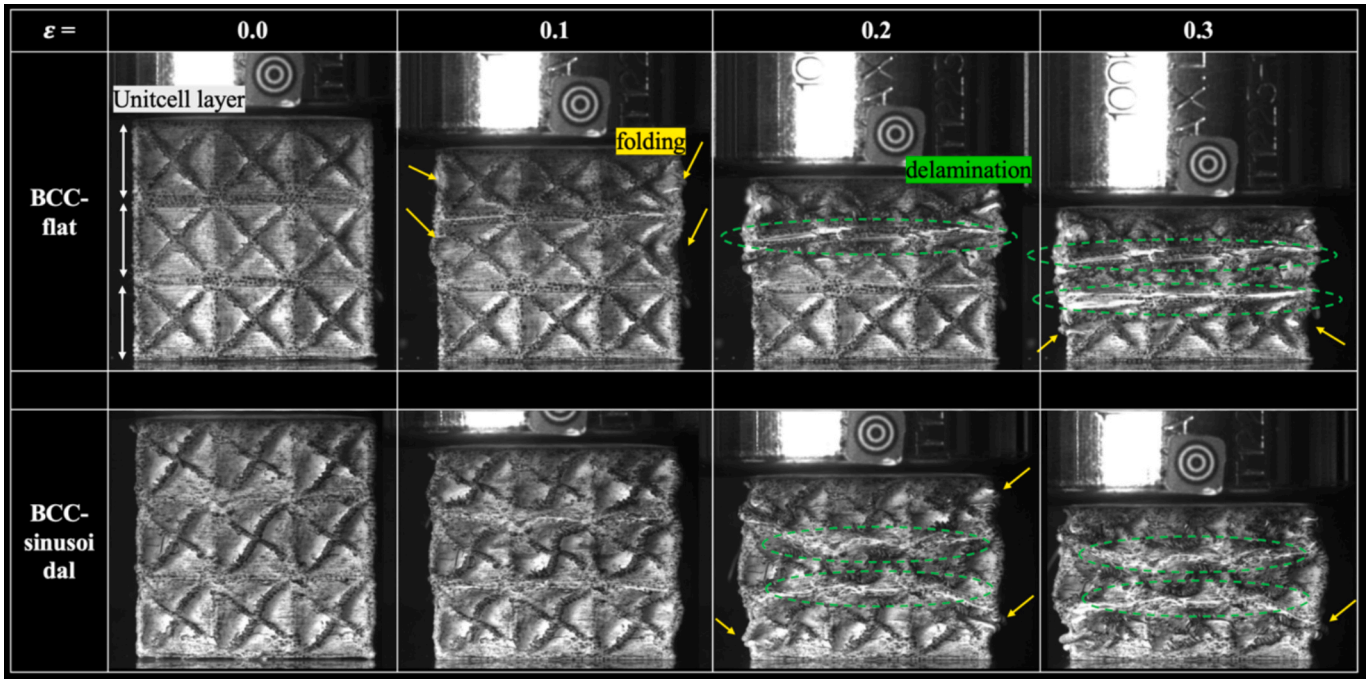


Fig. 9. Quasi-static compressive failure modes of BCC plate lattices with flat and sinusoidal geometries.

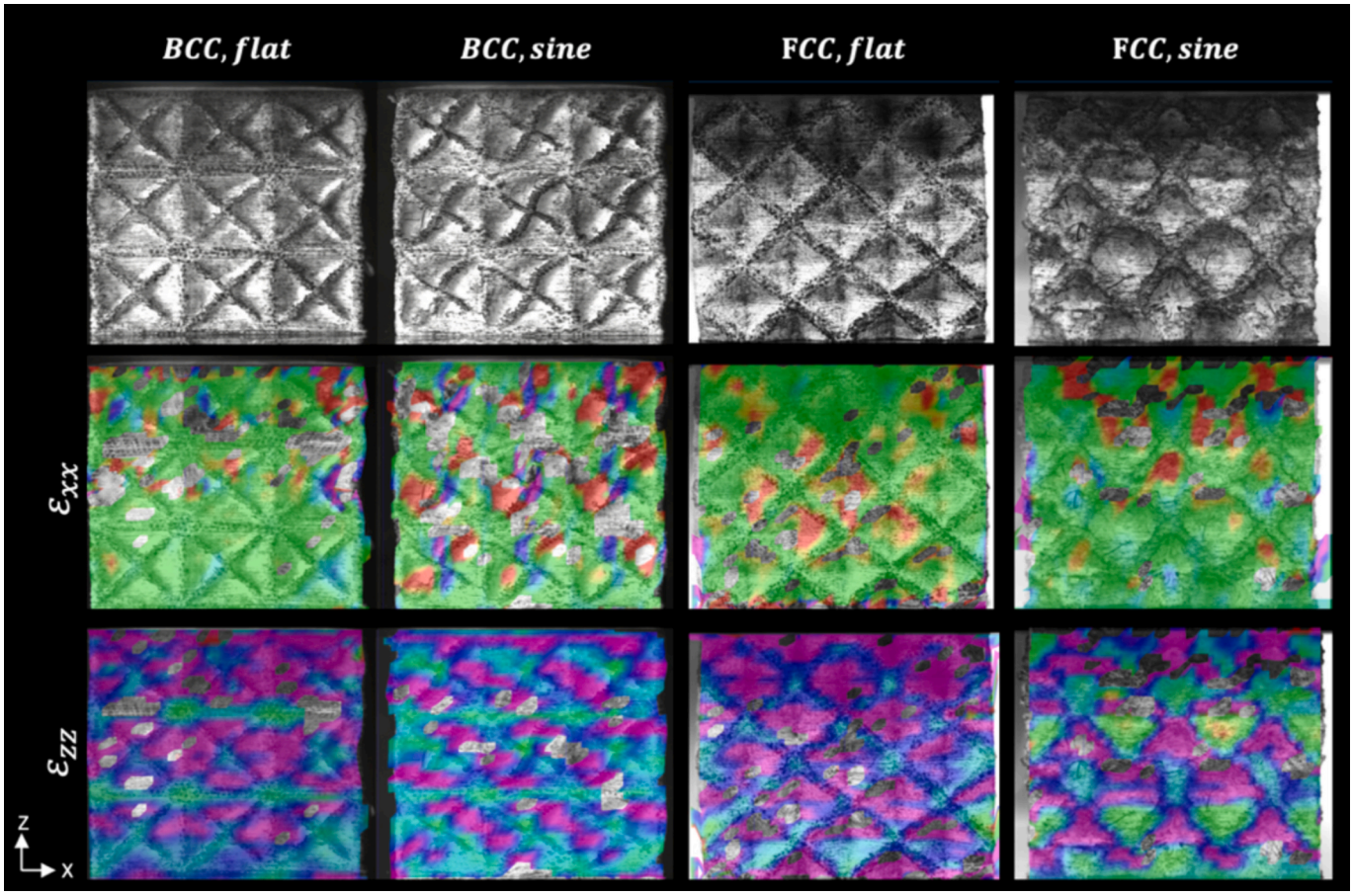


Fig. 10. Stain map from DIC results for each configuration at..$\varepsilon \approx 10\%$

deformation mode under compression. The ε_{zz} map revealed diagonal strain bands within individual unit cells (Fig. 10), and Fig. 9 showed subtle outward bulging at $\varepsilon = 0.1$ without the sharp folding seen in the flat BCC. While some interlayer delamination was still present, it was more diffuse and not confined to a single crack plane. These observations suggest that the sinusoidal geometry promoted out-of-plane

bending of the vertical plate. As these bending modes occurred repeatedly throughout the structure, they facilitated a more distributed plastic response. This shift is quantitatively supported by the increased power-law exponents for stiffness and strength scaling (Appendix C), which indicate a greater contribution from bending-dominated behaviour, consistent with delayed buckling reported for corrugated SC plate lattices [21].

Both flat and sinusoidal FCC lattices deformed through shear-dominated mechanism, as evidenced by global shear bands in the DIC strain maps (Fig. 10) and angular reorientation of plates (Fig. 11) [8]. While both exhibited minor qualitatively differences, their global deformation profiles diverged (Fig. 11). The flat FCC lattice developed a barrel-shaped profile with lateral expansion at mid-height, likely due to outward plate bending combined with frictional constraint at the platen–specimen interface, resulting in a mix of horizontal and vertical cracks. Conversely, the sinusoidal FCC lattice retained a more columnar form, with deformation confined along the loading direction and minimal visible cracking. Therefore, the sinusoidal plates likely inhibited lateral expansion, facilitating a more uniform axial load path. This behaviour corresponded with reduced stress fluctuations (Fig. 4), delayed onset of densification (Table 3), and slightly lower power-law exponents for stiffness and strength (Appendix C).

6.2. Failure mechanisms: dynamic regime

Failure modes under dynamic loading were broadly similar to those observed under quasi-static conditions (Fig. 12), but with increased brittleness. This is evidenced by sharper post-peak force drops in the dynamic curves (Fig. 5), consistent with trends reported in truss-based lattices [60]. The behaviour is likely associated with the viscoelastic nature of thermoplastic polymers such as ABS, where reduced chain mobility at elevated strain rates limits time-dependent plastic deformation and promotes a transition from ductile to brittle failure [61]. Additionally, greater force oscillations observed under dynamic loading may result from elastic wave propagation [62].

The flat and sinusoidal BCC lattices exhibited distinct failure modes under dynamic loading, which influenced their respective force–displacement responses. The flat variant reached a higher peak force but suffered a more pronounced subsequent drop, with failure initiating by buckling in the top unit-cell layer (Fig. 5a and 12c and d). In contrast, the sinusoidal variant failed from both ends, showing a lower average force and greater deformation. This reflects a trade-off between peak force and maximum displacement, as both configurations ultimately absorbed a comparable amount of energy.

While both FCC variants recorded similar peak forces (Fig. 5b), their post-yield failure modes diverged significantly (Fig. 12a and b). The flat FCC structure underwent abrupt failure through shear-localised collapse and fragmentation. Conversely, the sinusoidal FCC variant maintained structural integrity, deforming into a trapezoidal shape reminiscent of functionally graded systems [47], and dissipated impact energy through more distributed deformation.

Table 5 summarises the effects of introducing sinusoidal geometry into BCC and FCC plate lattices across different strain-rate regimes. Overall, the response reflects a structural trade-off: while the added geometric compliance reduces stiffness and strength, it enhances deformation stability and onset of densification. The effectiveness of this modification is governed by the dominant failure mechanism of the parent topology (i.e. bending- or stretching-dominated) and the applied strain rate. Sinusoidal BCC lattices exhibited more distributed failure and reduced strain-rate sensitivity, whereas sinusoidal FCC lattices benefited more under dynamic loading, showing suppressed fracture and enhanced strain rate sensitivity. Therefore, the performance of the sinusoidal modification depends jointly on structural failure mode and strain rate, offering a tuneable design strategy for specific application requirements.

7. Conclusions

This study systematically investigates the quasi-static and dynamic compressive response of plate lattices with varying relative density, unit cell type, and strain rate. Both conventional flat and novel sinusoidal plate geometries were examined in FCC and BCC configurations. The findings elucidate how geometric modification influences failure mechanisms and energy absorption in architected materials.

Flat BCC lattices showed a mixed bending and shear failure, with plastic hinges forming at the mid-span of the vertical {1 1 0} plates. Meanwhile, flat FCC lattices exhibited stretching-dominated failure with localised shear. These mechanisms aligned with the derived power-law

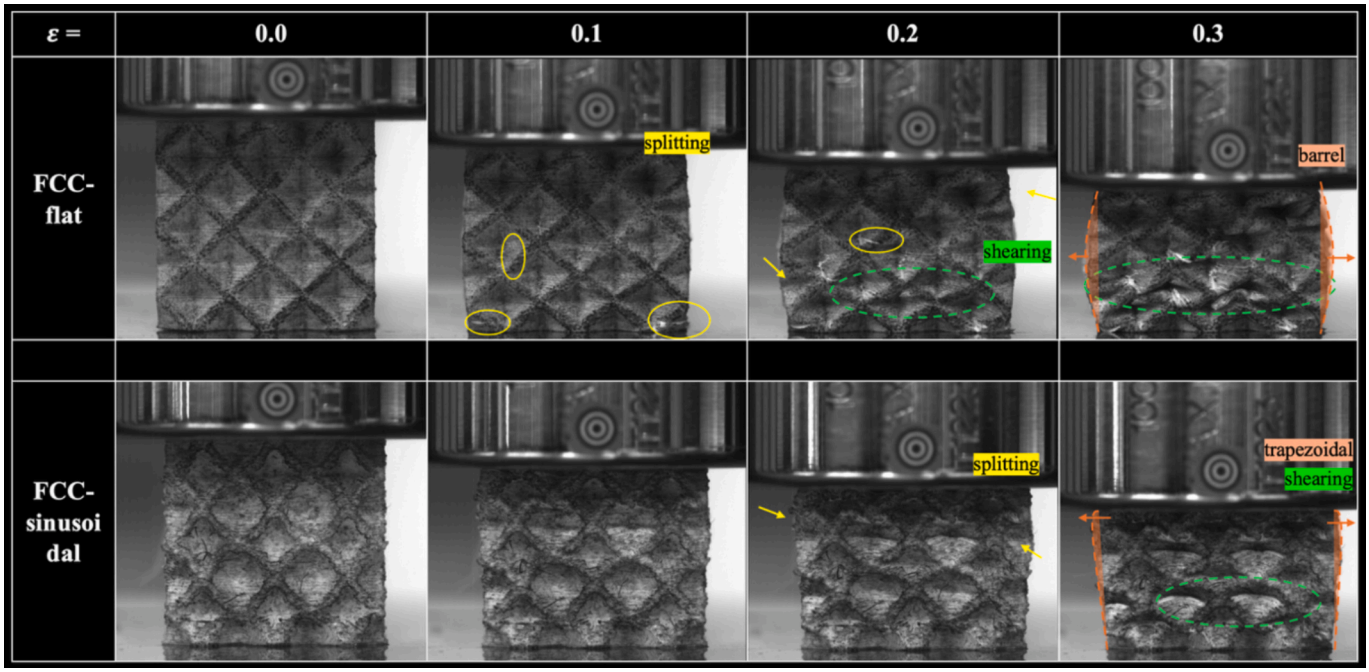


Fig. 11. Quasi-static compressive failure modes of FCC plate lattices with flat and sinusoidal geometries.

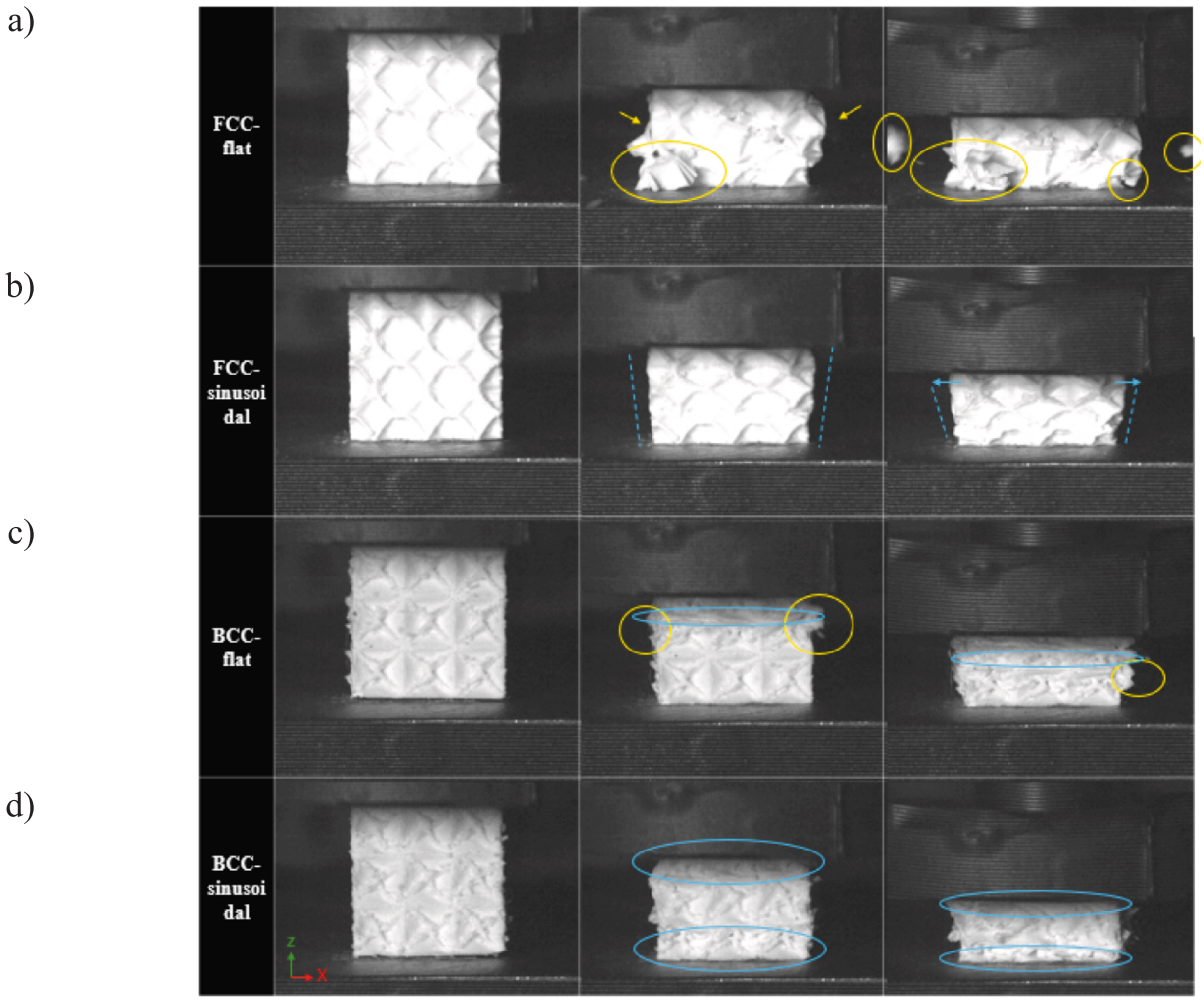


Fig. 12. Failure mechanisms under impact 60 J (yellow: localised failure; blue: layered/global failure). (For interpretation of the references to colour in this figure legend, the reader is referred to the web version of this article.)

Table 5
Summary of effects of sinusoidal modification on each cell types.

Parameter	Loading Regime	BCC Lattice (Sinusoidal)	FCC Lattice (Sinusoidal)
Baseline limitation	–	Prone to localised buckling due to vertical plate alignment	Susceptible to shear localisation under dynamic loading
Stiffness & strength	Q	Marked reduction	Moderate reduction
		Increased n_1, n_5 values	Reduced n_1, n_5 values
	D	Marked reduction	Comparable
Energy absorption	Q	Slightly decreased/comparable	Slight improvement/comparable
	D	Comparable	Comparable
Failure response	Q	Axial load redistribution; progressive collapse with less localisation	Delayed shear band formation; deformation more distributed
	D	Reduced peak force; more gradual collapse initiation	Extended plateau; less fluctuation; suppressed fractures
Strain rate sensitivity	–	Modest yield strength increases with strain rate	Noticeable yield strength increases with strain rate
Preferred application	–	Quasi-static deformation control	High-rate impact mitigation and energy absorption

Q: Quasi-static, D: Dynamic.
Exponents n_1, n_5 refer to stiffness and strength scaling with relative density (Table C1).

exponents. Introducing sinusoidal feature altered the failure mode, promoting distributed plastic deformation and suppressing localised failure, which resulted in smoother stress plateaus without reducing overall energy absorption.

The Cowper–Symonds model reliably predicted dynamic yield strength beyond the fitted strain-rate range. Classical plate theory was able to describe the buckling of flat plates but requires extension to capture sinusoidal geometries. Sinusoidal FCC lattices showed higher strain-rate sensitivity and strength gains compared to their flat counterparts, while this effect was less pronounced in BCC lattices.

Overall, this study demonstrates that the failure behaviour and mechanical performance of plate-based lattices can be tailored for intended strain rate regimes through geometric modification, providing a pathway for the development of impact-resistant architected materials. Future work should employ a greater number of tessellations to obtain more accurate homogenised properties, broaden the strain-rate range, and systematically examine the influence of printing parameters (e.g., build direction), constituent materials, and non-axial loading conditions

(e.g., oblique impact) to fully characterise the design implications. Numerical simulations incorporating rate-dependent plasticity would further clarify the deformation behaviour beyond experimental limits.

CRediT authorship contribution statement

Piyapat Jameekornkul: Writing – review & editing, Writing – original draft, Visualization, Validation, Methodology, Investigation, Data curation, Conceptualization. **Ajit Panesar:** Writing – review & editing, Supervision, Conceptualization.

Declaration of competing interest

The authors declare that they have no known competing financial interests or personal relationships that could have appeared to influence the work reported in this paper.

Appendix A

Estimation of critical impact velocity

The critical impact velocity was estimated to identify the threshold beyond which wave-dominated, non-equilibrium deformation is expected during dynamic loading. This was calculated using the relation

$$u_{cr} = \varepsilon_y \times c_e = \varepsilon_y \times \sqrt{E/\rho}$$

where ε_y is the quasi-static yield strain of the bulk material and c_e is the elastic wave speed [63]. For ABS, the elastic modulus $E = 1.22$ GPa and density $\rho = 1040 \frac{kg}{m^3}$ were used to compute the wave speed. The yield strain was estimated from $\sigma_y = 56MPa$ giving $\varepsilon_y \approx 0.0459$. Substituting into the equation gives a critical impact velocity of 49.7 m/s.

Appendix B

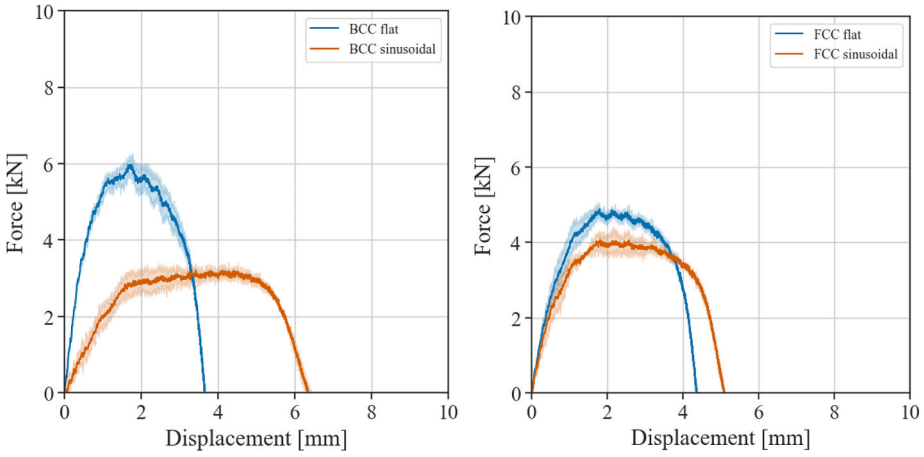


Fig. B1. Force-Displacement plots under impact energy 15 J (Left: BCC, Right: FCC).

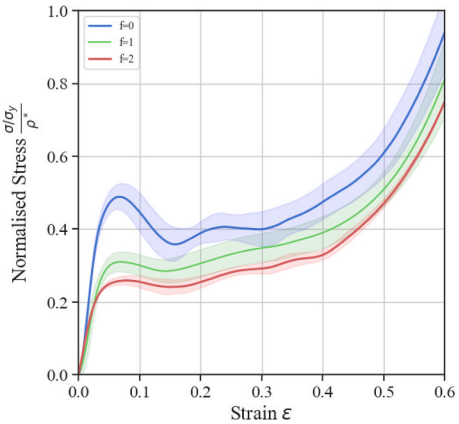


Fig. B2. Stress–strain plot under quasi-static loading shows the influence of f in BCC.

Appendix C

Table C1
Fitted power-law coefficients and corresponding errors.

UC type	Configurations	C_1	n_1	R^2	C_5	n_5	R^2
BCC	Flat	0.776	1.236	0.988	0.381	1.293	0.998
	Sinusoidal	0.651	1.403	0.989	0.309	1.398	0.999
FCC	Flat	0.620	0.999	0.999	0.289	1.061	0.998
	Sinusoidal	0.471	0.853	0.923	0.216	0.889	0.882

Table C2
Fitted coefficients and associated errors of Eq. (9) (Cowper–Symonds) obtained from experimental data, together with the Johnson–Cook model [59].

UC type	Configurations	Cowper-symonds			Johnson-cook	
		a	b	R^2	C_{JC}	R^2_{JC}
BCC	Flat	21.443	2.071	0.96	0.099	0.73
	Sinusoidal	134.808	3.148	0.99	0.069	0.96
FCC	Flat	40.203	2.117	0.95	0.072	0.73
	Sinusoidal	27.830	1.016	0.99	0.098	0.65
Bulk ABS		7464.094	6.169	0.94	0.062	0.99

Power-law coefficients

Plasticity model coefficients

Data availability

Data will be made available on request.

References

[1] N. Khan, A. Riccio, A systematic review of design for additive manufacturing of aerospace lattice structures: current trends and future directions, Prog. Aerosp. Sci. 149 (2024) 101021, https://doi.org/10.1016/j.paerosci.2024.101021.

[2] P. Ibrahim, P. Jameekornkul, A. Panesar, M.M. Attallah, The utility of additively manufactured β-Ti latticed hip implants in reducing femoral stress shielding: a finite element study, J. Mech. Behav. Biomed. Mater. 168 (2025) 106999, https://doi.org/10.1016/j.jmbbm.2025.106999.

[3] C. W. Isaac and F. and Duddeck, 'Current trends in additively manufactured (3D printed) energy absorbing structures for crashworthiness application – a review', *Virtual Phys. Prototyp.*, vol. 17, no. 4, pp. 1058–1101, Oct. 2022, doi: 10.1080/17452759.2022.2074698.

[4] M. Askari, et al., Additive manufacturing of metamaterials: a review, Addit. Manuf. 36 (2020) 101562, https://doi.org/10.1016/j.addma.2020.101562.

[5] J.B. Berger, H.N.G. Wadley, R.M. McMeeking, Mechanical metamaterials at the theoretical limit of isotropic elastic stiffness, Nature 543 (7646) (2017) 533–537, https://doi.org/10.1038/nature21075.

[6] T. Tancogne-Dejean, M. Diamantopoulou, M.B. Gorji, C. Bonatti, D. Mohr, 3D plate-lattices: an emerging class of low-density metamaterial exhibiting optimal isotropic stiffness, Adv. Mater. 30 (45) (2018) 1803334, https://doi.org/10.1002/adma.201803334.

[7] C. Crook, et al., Plate-nanolattices at the theoretical limit of stiffness and strength, Nat. Commun. 11 (2020) 1579, https://doi.org/10.1038/s41467-020-15434-2.

[8] D. Jiang, F. Ning, Physical-mechanical behaviors of stainless steel plate-lattice built by material extrusion additive manufacturing, J. Mater. Process. Technol. 309 (2022) 117739, https://doi.org/10.1016/j.jmatprotec.2022.117739.

[9] A. Karaki, A. Hammoud, E. Masad, M. Khraisheh, A. Abdala, M. Ouederni, A review on material extrusion (MEX) of polyethylene – challenges, opportunities, and future prospects, Polymer 307 (2024) 127333, https://doi.org/10.1016/j.polymer.2024.127333.

[10] J. Wu, et al., A hybrid architectural metamaterial combing plate lattice and hollow-truss lattice with advanced mechanical performances, Addit. Manuf. 76 (2023) 103764, https://doi.org/10.1016/j.addma.2023.103764.

[11] Z. Chen, Y.M. Xie, X. Wu, Z. Wang, Q. Li, S. Zhou, On hybrid cellular materials based on triply periodic minimal surfaces with extreme mechanical properties, Mater. Des. 183 (2019) 108109, https://doi.org/10.1016/j.matdes.2019.108109.

[12] L. Li, et al., Multifunctional hybrid plate lattice structure with high energy absorption and excellent sound absorption, Mater. Des. 241 (2024) 112946, https://doi.org/10.1016/j.matdes.2024.112946.

[13] Y. Zhu, J. Pan, E. Polyzos, J. Wang, L. Pyl, Design and numerical analysis of perforated plate lattice structures, Thin-Walled Struct. 204 (2024) 112339, https://doi.org/10.1016/j.tws.2024.112339.

[14] J.N. Heidenreich, M.B. Gorji, T. Tancogne-Dejean, D. Mohr, Design of isotropic porous plates for use in hierarchical plate-lattices, Mater. Des. 212 (2021) 110218, https://doi.org/10.1016/j.matdes.2021.110218.

[15] F. Wang, M. Brøns, O. Sigmund, Non-hierarchical architected materials with extreme stiffness and strength, Adv. Funct. Mater. 33 (13) (2023) 2211561, https://doi.org/10.1002/adfm.202211561.

[16] Y. Rong, J. Liu, W. Luo, W. He, Effects of geometric configurations of corrugated cores on the local impact and planar compression of sandwich panels, Compos. Part B Eng. 152 (2018) 324–335, https://doi.org/10.1016/j.compositesb.2018.08.130.

[17] I. Dayyani, A. D. Shaw, E. I. Saavedra Flores, and M. I. Friswell, 'The mechanics of composite corrugated structures: A review with applications in morphing aircraft', *Compos. Struct.*, vol. 133, pp. 358–380, Dec. 2015, doi: 10.1016/j.compstruct.2015.07.099.

[18] N.S. Ha, G. Lu, Thin-walled corrugated structures: a review of crashworthiness designs and energy absorption characteristics, Thin-Walled Struct. 157 (2020) 106995, https://doi.org/10.1016/j.tws.2020.106995.

[19] H. Wang, J. You, Y. Tian, Z. Chen, S. Yin, Dynamic mechanical behavior of sinusoidal corrugated dual-phase lattice metamaterials by additive manufacturing, Exp. Mech. 65 (4) (2025) 541–551, https://doi.org/10.1007/s11340-025-01160-7.

[20] V. Sundararaman, M.P. O'Donnell, I.V. Chenchiah, G. Clancy, P.M. Weaver, Stiffness tailoring in sinusoidal lattice structures through passive topology morphing using contact connections, Mater. Des. 226 (2023) 111649, https://doi.org/10.1016/j.matdes.2023.111649.

[21] J. Ding, et al., Imperfection-Enabled strengthening of ultra-lightweight lattice materials, Adv. Sci. 11 (41) (2024) 2402727, https://doi.org/10.1002/advs.202402727.

[22] F. Derveni, A.J. Gross, K.D. Peterman, S. Gerasimidis, Postbuckling behavior and imperfection sensitivity of elastic–plastic periodic plate-lattice materials, Extreme Mech. Lett. 50 (2022) 101510, https://doi.org/10.1016/j.eml.2021.101510.

[23] A.E. Medvedev, T. Maconachie, M. Leary, M. Qian, M. Brandt, Perspectives on additive manufacturing for dynamic impact applications, Mater. Des. 221 (2022) 110963, https://doi.org/10.1016/j.matdes.2022.110963.
[24] J.A. Hawreliak, et al., Dynamic behavior of engineered lattice materials, Sci. Rep. 6 (1) (2016) 28094, https://doi.org/10.1038/srep28094.
[25] P. Jameekornkul and A. Panesar, 'Dynamic behaviour of functionally graded lattice structures with short carbon fibre reinforcement', *Int. J. Impact Eng.*, p. 105525, Sept. 2025, doi: 10.1016/j.ijimpeng.2025.105525.
[26] T. Tancogne-Dejean, A.B. Spierings, D. Mohr, Additively-manufactured metallic micro-lattice materials for high specific energy absorption under static and dynamic loading, Acta Mater. 116 (2016) 14–28, https://doi.org/10.1016/j.actamat.2016.05.054.
[27] C. Lu, et al., Architectural design and additive manufacturing of mechanical metamaterials: a review, Engineering 17 (2022) 44–63, https://doi.org/10.1016/j.eng.2021.12.023.
[28] T. Tancogne-Dejean, X. Li, M. Diamantopoulou, C.C. Roth, D. Mohr, High strain rate response of additively-manufactured plate-lattices: experiments and modeling, J. Dyn. Behav. Mater. 5 (3) (2019) 361–375, https://doi.org/10.1007/s40870-019-00219-6.
[29] J.J. Andrew, J. Schneider, J. Ubaid, R. Velmurugan, N.K. Gupta, S. Kumar, Energy absorption characteristics of additively manufactured plate-lattices under low-velocity impact loading, Int. J. Impact Eng 149 (2021) 103768, https://doi.org/10.1016/j.ijimpeng.2020.103768.
[30] J.J. Andrew, P. Verma, S. Kumar, Impact behavior of nanoengineered, 3D printed plate-lattices, Mater. Des. 202 (2021) 109516, https://doi.org/10.1016/j.matdes.2021.109516.
[31] 'Lattice Planes and Miller Indices'. Accessed: Mar. 19, 2025. [Online]. Available: https://www.doitpoms.ac.uk/tlplib/miller_indices/index.php.
[32] I. Maskery, A.O. Aremu, L. Parry, R.D. Wildman, C.J. Tuck, I.A. Ashcroft, Effective design and simulation of surface-based lattice structures featuring volume fraction and cell type grading, Mater. Des. 155 (2018) 220–232, https://doi.org/10.1016/j.matdes.2018.05.058.
[33] A. Alhembar, J. Sheikh-Ahmad, F. Jarrar, S. Bojanampati, Optimizing the specific mechanical properties of lattice structures fabricated by material extrusion additive manufacturing, J. Mater. Res. Technol. 22 (2023) 1821–1838, https://doi.org/10.1016/j.jmrt.2022.12.024.
[34] 'UltiMaker S5', UltiMaker. Accessed: June 03, 2025. [Online]. Available: https://ultimaker.com/3d-printers/s-series/ultimaker-s5/.
[35] ASTM D20 Committee, *ASTM D695-23: Test Method for Compressive Properties of Rigid Plastics*. doi: 10.1520/D0695-23.
[36] ASTM E28 Committee, *ASTM E9-09: Test Methods of Compression Testing of Metallic Materials at Room Temperature*. doi: 10.1520/E0009-09.
[37] S. M. Walley and J. E. Field, 'Strain Rate Sensitivity of Polymers in Compression from Low to High Rates', *DYMAT J.*, 1994, [Online]. Available: https://www.icmm.ru/images/files/science/conferences/MIG-%D0%A1-26562/422StrWalleyDYMATJ1.pdf.
[38] S. P. Timoshenko and J. M. Gere, *Theory of Elastic Stability*. Courier Corporation, 2012.
[39] B. Budiansky, 'Theory of Buckling and Post-Buckling Behavior of Elastic Structures', in *Advances in Applied Mechanics*, vol. 14, C.-S. Yih, Ed., Elsevier, 1974, pp. 1–65. doi: 10.1016/S0065-2156(08)70030-9.
[40] J. Huang, R. Liu, J. Tao, Theoretical and numerical investigation of bicellular honeycomb under axial compression, Int. J. Crashworthiness 27 (3) (2022) 735–746, https://doi.org/10.1080/13588265.2020.1838159.
[41] T. Wierzbicki, Crushing analysis of metal honeycombs, Int. J. Impact Eng 1 (2) (1983) 157–174, https://doi.org/10.1016/0734-743X(83)90004-0.
[42] ASTM D30 Committee, *ASTM: D7136/D7136M: Test Method for Measuring the Damage Resistance of a Fiber-Reinforced Polymer Matrix Composite to a Drop-Weight Impact Event*. doi: 10.1520/D7136_D7136M-25.
[43] T. Maconachie, et al., SLM lattice structures: properties, performance, applications and challenges, Mater. Des. 183 (2019) 108137, https://doi.org/10.1016/j.matdes.2019.108137.
[44] L.J. Gibson, Cellular solids, MRS Bull. 28 (4) (2003) 270–274, https://doi.org/10.1557/mrs2003.79.
[45] Z. Hashin, S. Shtrikman, A variational approach to the theory of the elastic behaviour of multiphase materials, J. Mech. Phys. Solids 11 (2) (1963) 127–140, https://doi.org/10.1016/0022-5096(63)90060-7.
[46] J.L. Grenestedt, Effective elastic behavior of some models for perfect cellular solids, Int. J. Solids Struct. 36 (10) (1999) 1471–1501, https://doi.org/10.1016/S0020-7683(98)00048-1.
[47] J. Plocher, A. Panesar, Effect of density and unit cell size grading on the stiffness and energy absorption of short fibre-reinforced functionally graded lattice structures, Addit. Manuf. 33 (2020) 101171, https://doi.org/10.1016/j.addma.2020.101171.
[48] Y. Tian, X. Zhang, B. Hou, A. Jarlöv, C. Du, K. Zhou, Programmable heterogeneous lamellar lattice architecture for dual mechanical protection, Proc. Natl. Acad. Sci. 121 (43) (2024) e2407362121, https://doi.org/10.1073/pnas.2407362121.
[49] Y. Hou, C. Wen, K. Liu, J. Duan, H. Sun, Y. Guo, Local and global buckling prevention design of transformed triangular corrugated plates under shear and bending, Thin-Walled Struct. 211 (2025) 113135, https://doi.org/10.1016/j.tws.2025.113135.
[50] F. Derveni, F. Choquart, A. Abbasi, D. Yan, P.M. Reis, The most severe imperfection governs the buckling strength of pressurized multi-defect hemispherical shells, Mech. Mater. 204 (2025) 105295, https://doi.org/10.1016/j.mechmat.2025.105295.
[51] Z. Ye, V.L. Berdichevsky, W. Yu, An equivalent classical plate model of corrugated structures, Int. J. Solids Struct. 51 (11) (2014) 2073–2083, https://doi.org/10.1016/j.ijsolstr.2014.02.025.
[52] A. Gilat, R.K. Goldberg, G.D. Roberts, Strain rate sensitivity of epoxy resin in tensile and shear loading, J. Aerosp. Eng. 20 (2) (2007) 75–89, https://doi.org/10.1061/(ASCE)0893-1321(2007)20:2(75).
[53] X. Zhang, K. Zhang, B. Zhang, Y. Li, R. He, Additive manufacturing, quasi-static and dynamic compressive behaviours of ceramic lattice structures, J. Eur. Ceram. Soc. 42 (15) (2022) 7102–7112, https://doi.org/10.1016/j.jeurceramsoc.2022.08.018.
[54] X. Li, L. Xiao, W. Song, Compressive behavior of selective laser melting printed Gyroid structures under dynamic loading, Addit. Manuf. 46 (2021) 102054, https://doi.org/10.1016/j.addma.2021.102054.
[55] N. Jin, F. Wang, Y. Wang, B. Zhang, H. Cheng, H. Zhang, Failure and energy absorption characteristics of four lattice structures under dynamic loading, Mater. Des. 169 (2019) 107655, https://doi.org/10.1016/j.matdes.2019.107655.
[56] Y. Duan, B. Du, X. Shi, B. Hou, Y. Li, Quasi-static and dynamic compressive properties and deformation mechanisms of 3D printed polymeric cellular structures with Kelvin cells, Int. J. Impact Eng 132 (2019) 103303, https://doi.org/10.1016/j.ijimpeng.2019.05.017.
[57] M. A. Dundar, 'Exploring the strain rate influence on shear yield behavior of acrylonitrile-butadiene-styrene: Experimental and numerical study', *J. Thermoplast. Compos. Mater.*, p. 08927057241283339, Sept. 2024, doi: 10.1177/08927057241283339.
[58] G.R. Cowper, P.S. Symonds, Strain-hardening and strain-rate effects in the impact loading of cantilever beams, Defense Technical Information Center (1957), https://doi.org/10.21236/ad0144762.
[59] G.R. Johnson, W.H. Cook, 'A Constitutive Model and Data for Metals Subjected to Large Strains, High Strain Rates and High Temperatures', Proceedings of the 7th International Symposium on Ballistics (1983).
[60] A. Bouteldja, M.A. Louar, L. Hemmouche, L. Gilson, A. Miranda-Vicario, L. Rabet, Experimental investigation of the quasi-static and dynamic compressive behavior of polymer-based 3D-printed lattice structures, Int. J. Impact Eng 180 (2023) 104640, https://doi.org/10.1016/j.ijimpeng.2023.104640.
[61] B.Z. Jang, D.R. Uhlmann, J.B.V. Sande, Ductile–brittle transition in polymers, J. Appl. Polym. Sci. 29 (11) (1984) 3409–3420, https://doi.org/10.1002/app.1984.070291118.
[62] J. Cui, M. Zhao, Y. Zeng, F.B. Teshome, L. Chen, Z. Zeng, Evaluation of quasi-static and dynamic compressive properties of Ti-6Al-4 V functionally graded shell lattices with minimal surfaces, Mater. Today Commun. 40 (2024) 109792, https://doi.org/10.1016/j.mtcomm.2024.109792.
[63] C.J. Shen, G. Lu, T.X. Yu, Investigation into the behavior of a graded cellular rod under impact, Int. J. Impact Eng 74 (2014) 92–106, https://doi.org/10.1016/j.ijimpeng.2014.02.015.